Engineering 25 (2023) 182–193

Contents lists available at ScienceDirect

Engineering

journal homepage: www.elsevier.com/locate/eng

Research
Geodesy and Survey Engineering—Article

Ambient Noise Tomography for Coral Islands

Shaohong Xia [a,b,c,*], Changrong Zhang [a,b,c], Jinghe Cao [a,b,c]

[a] Key Laboratory of Ocean and Marginal Sea Geology, South China Sea Institute of Oceanology, Chinese Academy of Sciences, Guangzhou 510301, China
[b] Sanya Institute of Oceanology, South China Sea Institute of Oceanology, Sanya 572100, China
[c] Southern Marine Science and Engineering Guangdong Laboratory (Guangzhou), Guangzhou 511458, China

ARTICLE INFO

Article history:
Received 11 June 2021
Revised 13 September 2021
Accepted 29 September 2021
Available online 20 April 2022

Keywords:
Coral island
Ambient noise tomography
Engineering geology
South China Sea

ABSTRACT

As valuable land in the ocean, coral islands are not only important bases for making use of marine resources and protecting marine rights and interests, but also important for breakthrough research in many fields of earth science. Hence, the economical and efficient determination of the underground structure of coral islands has become significant in coral island engineering geology, but remains challenging for traditional marine geophysical prospecting and drilling methods. While ambient noise tomography with dense arrays has been widely used in continental regions, its applicability to coral islands remains undetermined. In this study, based on the data recorded by a dense array on an isolated coral island in the South China Sea, we analyzed the ambient noise characteristics and obtained a 3D subsurface structure of the coral island using ambient noise tomography. We made the following findings: ① The ambient noise frequencies can be roughly categorized into three levels: < 1, 1–5, and > 5 Hz. The spectral characteristics of the noise below 5 Hz were consistent at different stations, but there were significant differences in the characteristics of the noise above 5 Hz. ② For ambient noise frequencies below 5 Hz, cross-correlation functions with high quality could be obtained with only 24 h of waveform data. However, it was difficult to extract meaningful cross-correlation functions for ambient noise frequencies above 5 Hz. ③ The surface-wave velocity in the coral island was higher toward the sea and lower toward the lagoon, which was consistent with the high degree of cementation of the outer reef flat stratum on the seaward side. ④ There were two low-velocity horizons at depths of 25–75 and 200–300 m, which were in good agreement with the high-porosity horizons that were revealed by drilling core samples, reflecting the weathering history of the reef. Our research demonstrates that ambient noise tomography is a potentially economical, efficient, and environmentally friendly method for the geological prospecting of coral reefs.

1. Introduction

Coral islands can be thought of as the oases of the marine "desert." As an extremely valuable land resource, they are essential for marine resource management and the protection of marine rights and interests [1,2]. In addition, as a unique geological unit formed by the joint action of marine organisms and geological activity, they are important nodes of connectivity between the lithosphere, hydrosphere, and marine biosphere [3,4] and a repository of information on regional tectonic evolution and global environmental change [5]. With the increasing need to make use of offshore oil, natural gas, and fishery resources and to construct infrastructure, the scale of reef engineering construction continues to grow. To meet the needs of this industry, there is an urgent need to conduct detailed studies on the fine subsurface structure of coral islands [6]. The strata of coral reef islands are composed of different materials than terrestrial substrates, being primarily composed of reef limestone and bioclastic sediment—a weakly cemented layer comprising bioclastic sand and gravel that includes fragments of corals, mollusks, calcareous algae, and so on [2,7]. The reef limestone is formed from the skeletons of dead coral groups that have grown *in situ*. During its formation, due to changes in climate, sea level changes, or crustal subsidence and uplifting, loose gravel layers and general unconformities are developed in the reef limestone, and holes and karst caves often appear [8,9]. The special strata and diagenesis of coral islands make their geological structure complex and dynamic, with significant lateral inconsistencies, and prone to geological events such as collapse, landslides, and earthquakes [10,11]. Therefore, the effective detection and imaging of the subsurface structures of coral islands has become an important field of research in engineering geology [6,12].

* Corresponding author.
E-mail address: shxia@scsio.ac.cn (S. Xia).

https://doi.org/10.1016/j.eng.2021.09.022

For many years, traditional marine geophysical exploration methods, such as seismic reflection, side-scan sonar, multibeam, and acoustic techniques, have been widely used to survey the subsurface structure of coral reefs. These methods have been successfully used to study submarine topography [13,14], sedimentary characteristics [15–17], carbonate hydrocarbon accumulation and evolution [18,19], fault distribution [20], and submarine landslides [21,22]. However, these technologies are generally limited to areas with water depths of more than 20 m, making it challenging to survey shallow lagoons and exposed surfaces. Thus, most of our current knowledge on coral island bodies comes from drilling data that can only provide point information [23–25], which limits the resolution of three-dimensional (3D) subsurface coral island maps. In addition, drilling and artificial seismic exploration is expensive, and field operation processes are cumbersome. Therefore, there is a need to develop an efficient and economical imaging methodology that suits the unique geological attributes of coral islands and the acquisition of 3D subsurface maps of these areas.

Ambient noise tomography, which uses ambient seismic noise to characterize the surface-wave (S-wave) attributes of the substrate, is economical and attractive to many geophysicists [26–29]. In recent years, with the development of dense arrays, the effectiveness of using ambient seismic noise tomography to investigate subsurface structures at fine resolutions has been recognized [30–32]. This methodology has been successfully applied to fault zone imaging [33,34], geothermal reservoir imaging [35,36], hydrological studies [37,38], and geological hazard prevention and mitigation contexts [39]. In the ocean, empirical cross-correlation functions have been retrieved from ocean-bottom seismometer pairs, whose interstation distance are tens to hundreds of kilometers, at a range of periods from 1 to a few hundred seconds, and the structure of the crust and uppermost mantle has been studied [40–42]. Ambient noise tomography extracts S-wave empirical cross-correlation functions from the continuous seismic waveforms between station pairs to study the subsurface structure, so its successful application is closely tied to the ambient seismic noise attributes of the study site. Coral island strata are uniquely isolated in the ocean, with noise sources that are significantly different from those of continents and the ocean floor. What characterizes coral island ambient noise? Can this ambient noise be used for imaging purposes? If so, what noise frequency band is appropriate for imaging? How long data must be recorded to obtain cross-correlation functions with high signal-to-noise ratios (SNRs)? What are the characteristics of the S-wave structure in coral islands? What tectonic information on coral islands can the S-wave structure supply? Further study is needed to answer these questions.

In this study, we set up a dense seismic array on an isolated coral island in the South China Sea (Fig. 1(a)) and applied ambient noise tomography to the recordings. From the continuous 5-day-long seismic noise waveform data we collected, we obtained cross-correlation functions with high SNRs and used them to produce a 3D subsurface geological map of the coral island at the study site. Here, we discuss the structural characteristics and genetic mechanisms of the low-velocity bodies of the island, using drilling core samples as a comparative method. Our research effectively evaluates the feasibility of using ambient noise tomography to map the subsurface geological structure of a coral island.

2. Data and ambient noise analysis

2.1. Data

A dense array comprising 43 portable seismic instruments, with a corner frequency of 5 s for all three components, was deployed on an isolated coral island in the South China Sea (Fig. 1(a)) from 5 to 9 January 2019. The stations were distributed along the coral island, covering an area of approximately 300 m × 2000 m (north–south × east–west). The array was sandwiched between the deep sea and lagoon on the southwest and northeast sides, respectively. The average station spacing was approximately 100 m, and the sampling rate was set to 100 samples per second for all stations. To ensure the acquisition of good-quality data and the safety of the stations, all instruments were buried approximately 10 cm below the surface (Fig. 1(b)). Over the 5-day-long deployment period, the northeast monsoon conditions in the South China Sea were intense, with strong winds and waves. Two of the instruments failed to record usable data due to failure, so 41 datasets of good quality were acquired.

2.2. Frequency spectrum of coral island ambient noise

The daily frequency spectrograms for the data from the 41 good-quality datasets were first calculated (Figs. 2(a)–(e)). As depicted in the figure, they revealed that ① the ambient noise recorded at the coral island can be divided into three frequency categories: < 1, 1–5, and > 5 Hz, with the amplitudes of frequencies increasing in the following order: 1–5, > 5, < 1 Hz; ② the ambient noise was relatively stable over the observation period, and the frequency spectrogram characteristics were consistent across each day; and ③ across stations, ambient noise frequencies below 5 Hz were generally consistent, while those above 5 Hz varied widely, indicating that the source of the former and latter were likely regional and local, respectively.

2.3. Cross-correlation functions of coral island ambient noise

The first stage of ambient noise tomography involves the cross-correlation of ambient noise waveforms between each dataset. Our

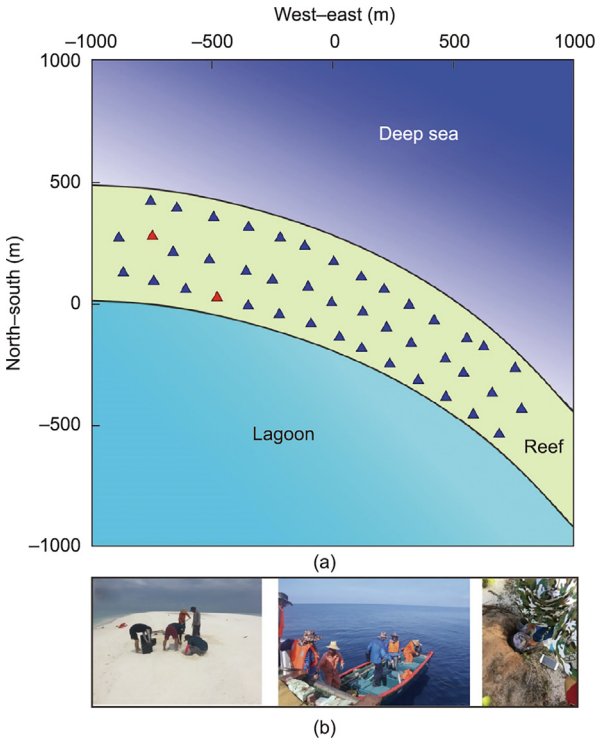

Fig. 1. (a) Distribution of the seismic stations (triangles) on the coral island, with red triangles depicting faulty stations; the coral island is located in the southern South China Sea. (b) Installation pictures of our stations.

methodology followed that of Bensen et al. [43]. Continuous waveforms were cut into 1 h segments; they were then demeaned and detrended, and spectrum whitening and waveform normalization were applied. Cross-correlation, with a maximum lag time of 10 s, was then conducted on each segment, and the final cross-correlation functions were obtained by superimposing the results from this step over each other [44]. The cross-correlation functions for the vertical waveforms for 5 January 2019, at 0.2–1.0, 1.0–5.0, and 5.0–10.0 Hz, are respectively shown in Figs. 2(f)–(h). They show that the cross-correlation function of the ambient noise

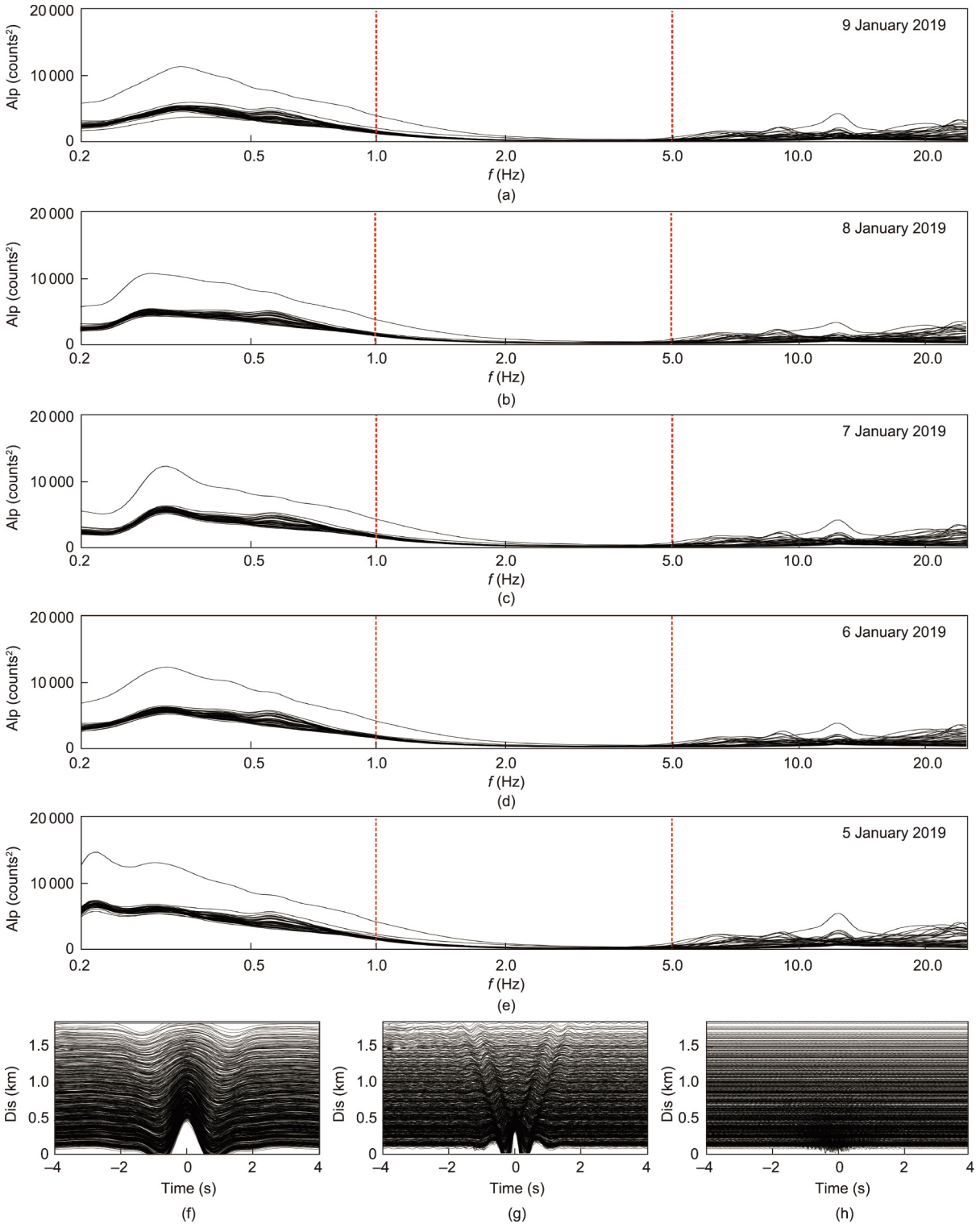

Fig. 2. (a–e) Ambient noise frequency (*f*) spectrograms of 41 stations from 5 to 9 January 2019, respectively; (f–h) cross-correlation functions derived from the vertical waveforms recorded on 5 January 2019 at (f) 0.2–1.0 Hz, (g) 1.0–5.0 Hz, and (h) 5.0–10.0 Hz, respectively. (f) and (g) subplots also illustrate signals with positive and negative lag for small interstation distances, which can interfere with accurate calculation of the cross-correlation functions. Alp: amplitude; Dis: distance.

below 5 Hz was of very good quality, and that a clear seismic phase could be observed. In contrast, the cross-correlation functions for the 5–10 Hz spectrums did not show an obvious seismic phase. Our analysis of the frequency spectrograms from different stations (Figs. 2(a)–(e)) indicates that the noise sources that are below 5 Hz are regional. It should be mentioned that for closely spaced station pairs, signals with positive and negative lag can interfere with each other over long periods of time, rendering the dispersion curves unreliable [29]. As shown in Fig. 2(f), although a clear Rayleigh waveform is visible for the cross-correlation functions at 0.2–1.0 Hz, it was difficult to obtain reliable dispersion curves because of low signal frequencies. Therefore, in this study, we mainly used the cross-correlation functions at 1–5 Hz for ambient noise tomography.

2.4. Influence of continuous observation time on cross-correlation functions

The cost and efficiency of exploration are directly determined by the duration of field operations. To identify any possible links between the length of observation and the cross-correlation functions, we calculated the cross-correlation functions using continuous 1 h, 12 h, 1 d, and 5 d waveform segments, at 1–5 Hz. We found that a less obvious seismic phase could be observed in the cross-correlation functions (Fig. 3(a)) obtained from the 1 h segments. The seismic phase in the cross-correlation functions obtained from the 12 h segments (Fig. 3(b)) was relatively clearer and continued to become more evident as the segment duration extended. Thus, the seismic phase was more obvious in the cross-correlation functions obtained from 1- and 5-day-long segments (Figs. 3(c) and (d)). Our calculations of the SNR of the cross-correlation functions are shown in Fig. 4. Here, the SNR is defined as the ratio of the maximum amplitude in the signal window (from −4 to 4 s) to the average absolute amplitude of the noise window (from −10 to −4 s and 4–10 s) of the cross-correlation function. The SNRs of the 1 h, 12 h, 1-day-long, and 5-day-long cross-correlation functions were 4–13, 10–30, 13–40, and 20–60, respectively, indicating that the SNR of the cross-correlation functions increased with increases in segment duration (i.e., observation time). The SNR consistently decreased with increases in the interstation distance (Fig. 4) for all segment durations.

The symmetry of the cross-correlation functions can indicate the azimuth of the noise source: The greater the symmetry, the more uniform the distribution of the noise sources, and vice versa [45]. We used the ratio of the maximum absolute amplitude of the positive window of the cross-correlation function (0–10 s) to the maximum absolute amplitude of the negative window (from −10 to 0 s) to characterize symmetry. The closer the amplitude ratio was to 1, the stronger the symmetry. As shown in Fig. 5, the amplitude ratios of the correlation functions were mainly concentrated between 0.5 and 1.5. The amplitude ratios converged to 1 as the segment duration increased, and the symmetry of the 5-day-long cross-correlation functions was the greatest. This finding indicates that longer observation periods result in more uniform noise source distributions. The results of the symmetry analysis showed that the distribution of 1–5 Hz noise sources at the coral island was uniform, and there was no obvious directional variation during the observation period.

3. Method and results

3.1. Method

The cross-correlation functions derived from the 5-day-long 1–5 Hz waveform segments were subsequently averaged across the positive and negative lag, to improve their SNRs. From these, we obtained 189 cross-correlation functions from interstation distances larger than 1 km (Fig. 6(a)). Multiple filter techniques were applied to the cross-correlation functions to obtain the dispersion curve of the Rayleigh group velocities between 0.2 and 0.5 s [46]. Group velocity dispersions with interstation distances less than 1.5 times the wavelength were rejected. As shown in Fig. 6(b), the group velocities were mainly distributed in the range of 1.2–1.9 km·s^{-1}, with an average of approximately 1.4 km·s^{-1}. The number of data points ranged from 161 to 189. The strong fluctuation of the group velocity dispersion curves (1.2–1.9 km·s^{-1}) may indicate that the velocity of the reef is significantly horizontally heterogeneous. Therefore, we classified the dispersion curves into three

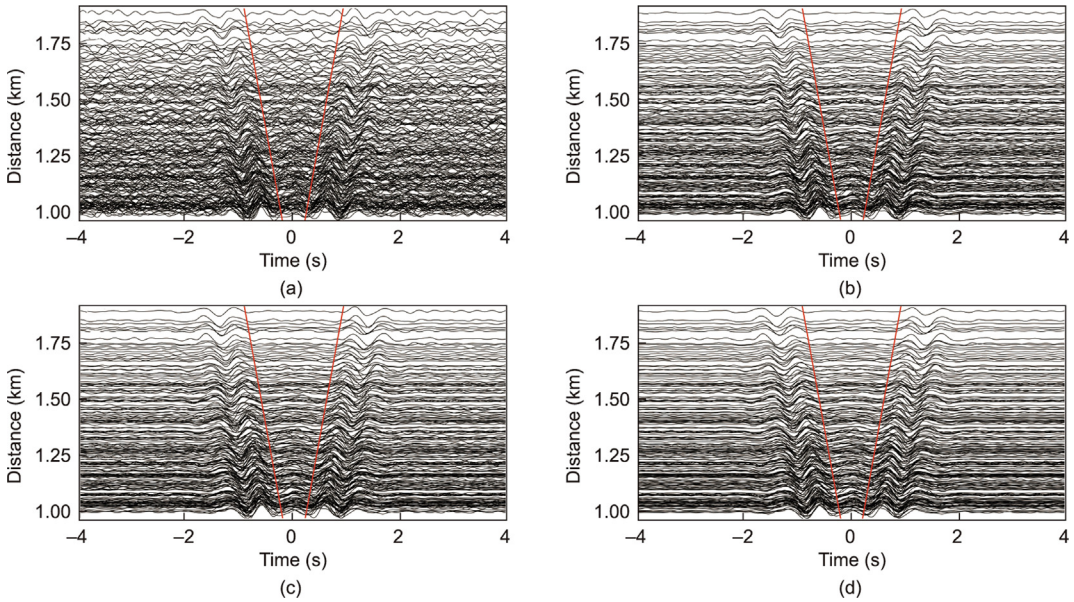

Fig. 3. Cross-correlation functions derived from (a) 1 h, (b) 12 h, (c) 1 d, and (d) 5 d segments. The red lines show the reference velocity of 1.3 km·s^{-1}.

parts according to their ray paths (Fig. 6(c)) as follows: ① rays that propagate on the outer reef (red); ② rays that propagate on the inner reef (blue); and ③ rays that propagate on both the outer and inner reef (black). It was found that the group velocity of the rays passing through the outer reef was greater than the average group velocity, while the group velocity of the rays passing through the inner reef was less than the average group velocity (Fig. 6(b)), which implied that the S-wave velocity (S-wv) of the outer reef was greater than that of the inner reef.

We then applied a subspace inversion algorithm to the Rayleigh wave group velocity data at 0.2–0.5 s periods, using an iterative nonlinear tomographic method with fast marching [47]. Since the straight-ray assumption of surface wave propagation no longer holds in a strongly horizontally heterogeneous media, the fast-marching method can account for the ray path bending away from the path of a straight ray and could improve the imaging results [47]. After obtaining the group velocity maps for different periods, the 3D S-wv structure of the coral island was determined using the linear inversion method [46], by dividing the inversion model into 20 m deep layers.

3.2. Results

Checkerboard resolution tests were first conducted to evaluate the horizontal resolution of the group velocity tomographic results. We assigned positive and negative velocity anomalies (±0.1 km·s^{-1}) with a size of 150 m × 200 m to the average group velocity model (Fig. 7(a)) to establish the checkerboard model and calculate corresponding synthetic arrival times. The numbers of stations and rays in the synthetic data were the same as those in the real dataset (Fig. 7(b)). Then, we inverted the synthetic data to test the obtained checkerboard results. Restricted by the spatial distribution of the stations, the azimuth of the ray data was mainly west northwest–east southeast (WNW–ESE) oriented (Figs. 6(c) and 7(b)), and the checkerboard test results were slightly smeared in a WNW–ESE direction. But, the group velocity checkerboard pattern was reliably recovered in the ray coverage area (Figs. 7(c)–(f)), indicating that the data used in our study can be used to reveal the horizontal variations that are characteristic of coral islands.

The group velocity results for the 0.2, 0.3, 0.4, and 0.5 s periods are shown in Figs. 8(a)–(d), respectively. The subsurface structures of the island are horizontally inhomogeneous, higher on the seaward side (northeast side), and lower on the lagoon side (southwest side) for all periods. The low-velocity anomalies were further divided into northwest and southeast sections. The S-wv inversion results are shown in Fig. 9. We plotted the horizontal slices of the S-wv structures at depths of 0–400 m (Fig. 9(a)), according to the depth-sensitivity kernels for the 0.2–0.5 s Rayleigh wave group velocity dispersions of the S-wvs (Fig. 9(d)). The 3D S-wv structures were generally characterized by high velocities in the seaward (northeast) side and low velocities in the lagoon-ward (southwest) side. Their S-wv range was about 1.3–1.8 km·s^{-1}, which was consistent with the S-wv range (approximately 1.2–2.3 km·s^{-1}) of the core samples above depths of 160 m

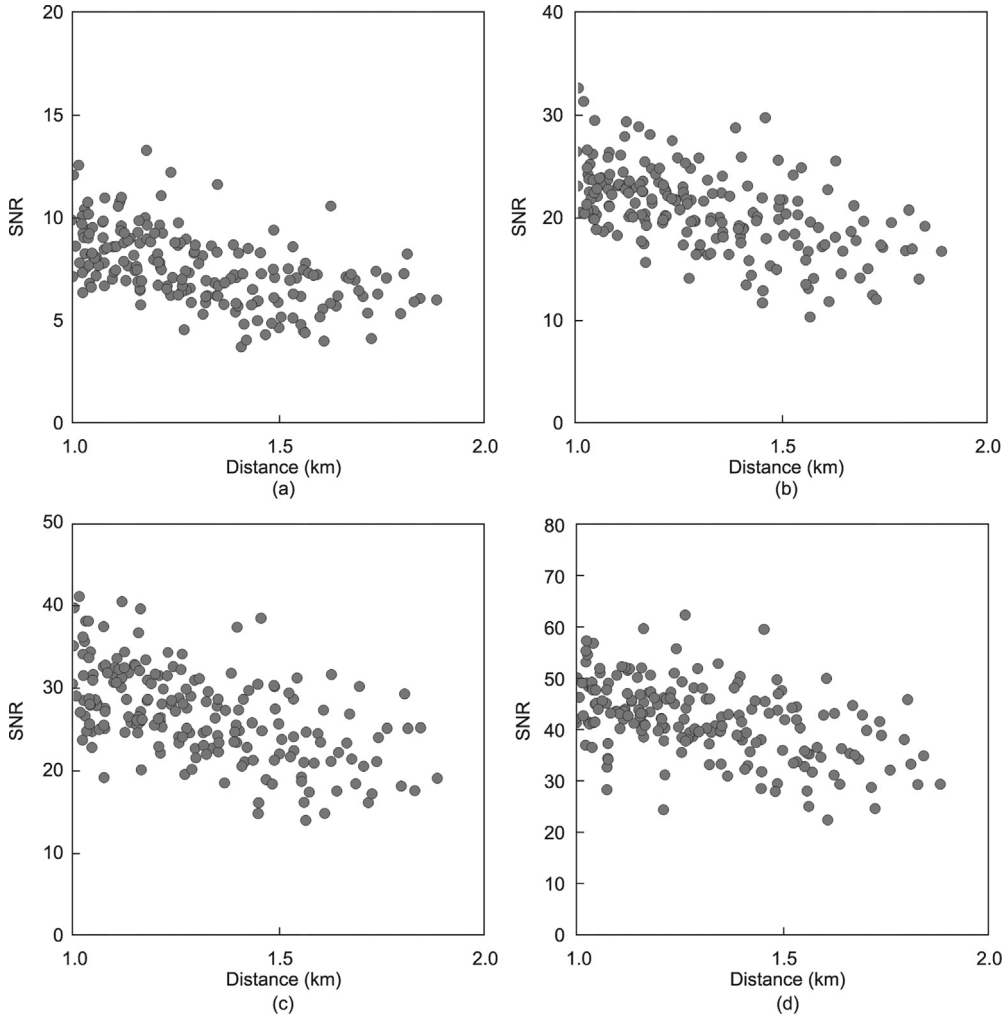

Fig. 4. SNR of the (a) 1 h, (b) 12 h, (c) 1 d, and (d) 5 d cross-correlation functions. The general trend is for the SNR to decrease with an increase in the interstation distance.

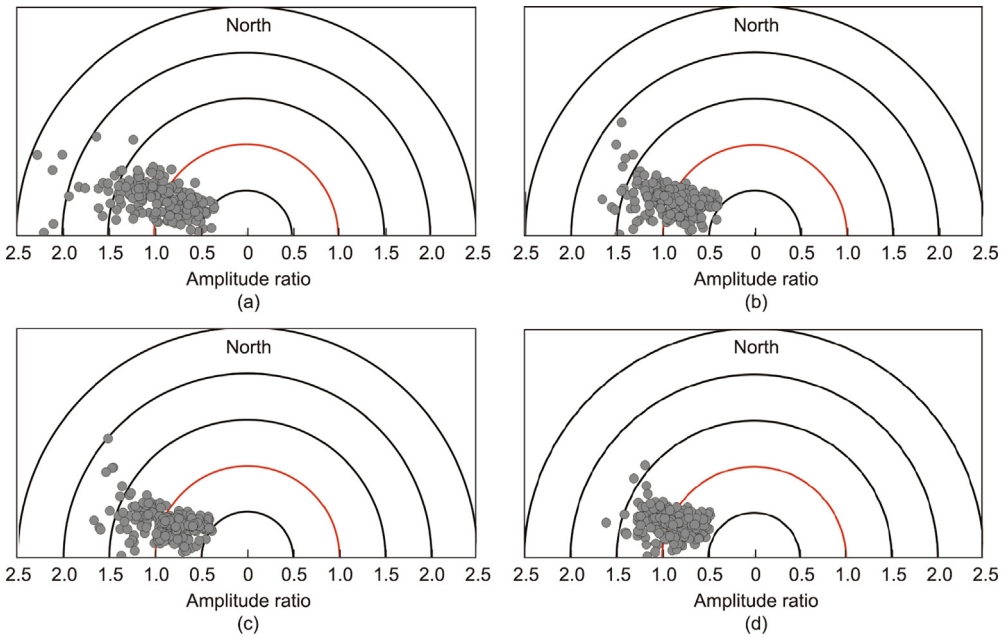

Fig. 5. Amplitude ratios for positive and negative windows of cross-correlation functions derived from (a) 1 h, (b) 12 h, (c) 1 d, and (d) 5 d segments.

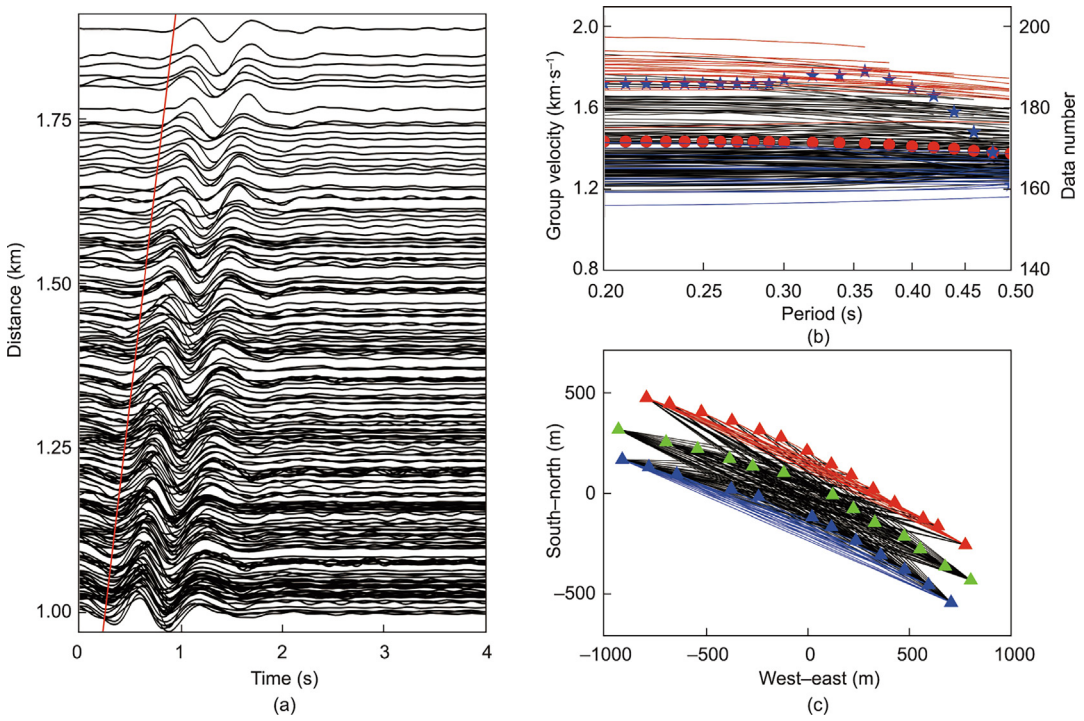

Fig. 6. (a) 5-day-long cross-correlation functions, averaged by positive and negative lags, at 1–5 Hz. The red lines show the reference velocity of 1.3 km·s^{-1}. (b) Dispersion curves derived from the cross-correlation functions shown in (a); red, blue, and black lines are the dispersion curves of the rays that propagate on the outer reef, inner reef, and whole reef in (c), respectively. Red circles indicate the average dispersion curve, and blue stars are the number of data points at 0.2–0.5 periods. (c) Stations and rays of the dispersion curves; triangles indicate the stations, while red, blue, and black lines are the rays that propagate on the outer reef, inner reef, and whole reef, respectively.

in the NY-1 well in the South China Sea [48], indicating the reliability of our results. A comparison of the horizontal slices of different depths revealed a distinct structural contrast between the high- and low-velocity anomalies above a depth of 200 m. With an increase in depth, the differences between the high- and low-velocity anomalies of the reef gradually decreased, indicating that the lateral differences of the island also gradually disappear with depth.

There is a well on the study coral island, and its core samples showed that there are obvious differences in strata porosity at different depths, among which there are two relatively high porosities (approximately 60%) at 25–75 and 200–300 m (Fig. 9(c)). Our constructed S-wv structures showed low-velocity anomalies at the same depths (Fig. 9(b))—a result that was consistent with the core sample porosities. The checkerboard test results (Fig. 7)

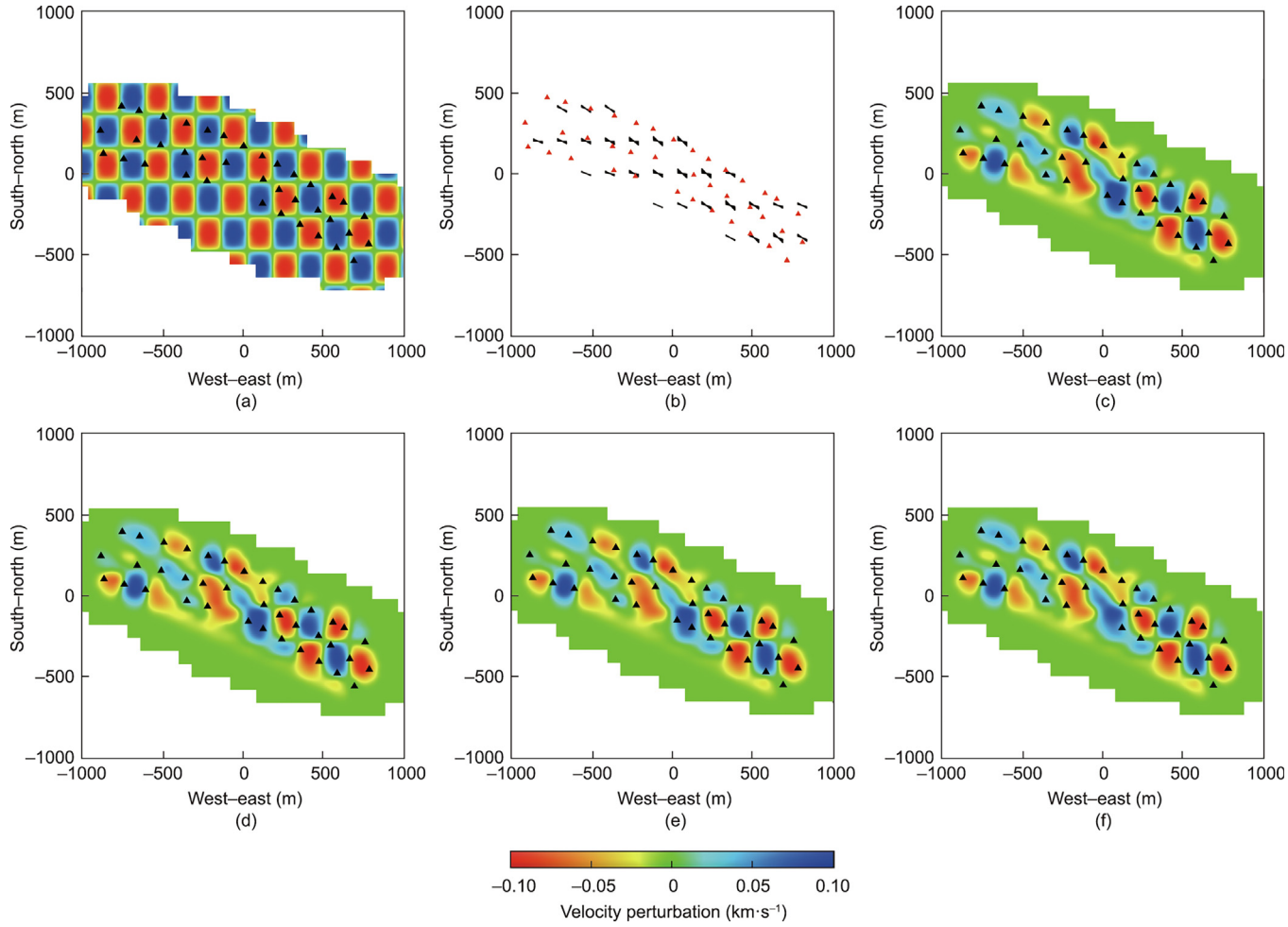

Fig. 7. (a) Checkerboard model; (b) azimuthal coverages of the rays at each grid; (c–f) checkerboard results at (c) 0.2, (d) 0.3, (e) 0.4, and (f) 0.5 s periods, respectively. The triangles in the figure indicate the stations used with the inversion algorithm.

and depth–sensitivity kernels (Fig. 9(d)) also showed that these two low-velocity layers are reliable. The good correspondence between the high porosities and the low-velocity anomalies indicates that the S-wave models obtained by ambient noise tomography can accurately reflect the subsurface material composition and reveal the weak structural layers in the coral reef.

4. Discussion

4.1. Coral reef geological structure revealed by ambient noise tomography

The shallow strata of coral reefs, which are mainly composed of bioclastic sediment and reef limestone, is the main focus of coral reef engineering geology. Bioclastic sediment is a weakly cemented sedimentary layer formed from bioclastic sand and gravel, including fragments of corals, mollusks, calcareous algae, and so on [2,7]. Bioclastic sediments generally develop from reef flats to lagoons, in which the outer reef flat sediment is primary reef with a high degree of cementation, and the sediment in the lagoon is mainly composed of consolidated coral detritus [8,49]. The reef limestone is formed from the skeletons of the dead coral that grew *in situ*. In the process of reef limestone formation, climate and sea level changes or coral reef subsidence and uplifting often result in the loosening of gravel layers and the development of unconformities such as holes and karst caves [8,9]. The distribution and degree of cementation in bioclastic sediment and reef limestone are the key factors determining the stability of coral islands.

The 3D S-wv structures we obtained revealed the state of the substratum and the weaknesses in the structure of the stratum across the coral reef. Spatially, the northeast face of the coral reef is close to the deep sea, and the southwest side is close to the lagoon (Fig. 1(b)). The S-wvs of the coral reef were higher in the northeast and lower in the southwest (Figs. 8 and 9(a)), which is consistent with the evolutionary features of the coral reef stratum from the outer reef flat to the lagoon, where the primary state and extent of the stratum cementation gradually decrease. Vertically, the drilling core samples revealed that there are two layers with high porosity at depths of 25–75 and 200–300 m (Fig. 9(c)), which is consistent with the low S-wv anomalies (Fig. 9(b)). The petrology and geochemistry of the 0–220 m core samples showed that the coral reef stratum in the study region has mainly been controlled by regional sea level changes. The decrease in the sea level of the South China Sea at approximately 0.23–0.90 mega annum (Ma) resulted in stagnation in the growth of the coral reefs and exposed the stratum to precipitation [50]. Thus, the reef limestone was eroded, which caused the porosity to increase, resulting in a decrease in the seismic wave velocity at depths of 25–75 m (Fig. 10).

Although the low-velocity anomalies at depths of 200–300 m were consistent with the high porosities of the drilling core samples (Figs. 9(b) and (c)), our imaging results showed that anomalies did not develop throughout the whole coral reef but are only clear

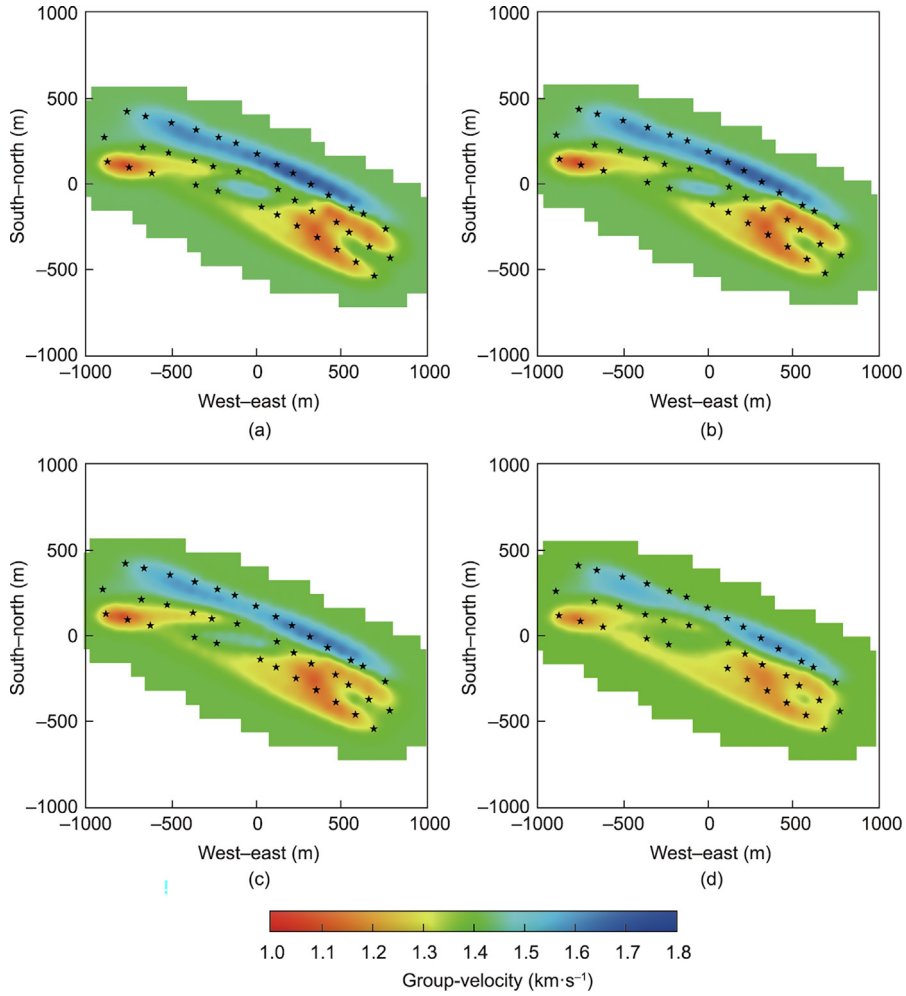

Fig. 8. Plotted group velocity inversion results for the (a) 0.2, (b) 0.3, (c) 0.4, and (d) 0.5 s periods, where black stars indicate the stations used in the inversion.

in local areas (Fig. 10); this finding is in contrast to the low-velocity anomalies at depths of 25–75 m. The AA′ profile of the outer reef flat (Fig. 10(b)) showed that the S-wvs reverse at a depth of approximately 200 m, and the S-wvs at depths of 75–200 m are higher than those at depths greater than 200 m. Previous studies have shown that the strata of the outer reef flat are mainly composed of primary reefs, where the sedimentary cementation increases with depth [8,9,49]. In the absence of geological events, the strata S-wv should also lack obvious deep low-velocity reversions. Our results revealed an obvious low-velocity reversion phenomenon in the outer reef flat at a depth of 200 m, which should be indicative of strata exposure, erosion, and weathering events during the reef's history. Because the stratum at depths of 200–300 m formed earlier than that at depths of 25–75 m, it experienced more intense—and possibly lateral—forces during its compaction after deposition, which produced lateral heterogeneity in low velocities at depths of 200–300 m.

Previous studies have shown that multiple sea-level-change events have occurred in the South China Sea since the early Miocene [24–26]. We speculate that the low-velocity reversions in the 200–300 m stratum may be the geological footprint of one of these sea-level-change events. It should be noted that data sensitivity decreases with increases in depth (Fig. 9(d)). Hence, the image results for depths of 200–300 m are relatively smoother than those of the shallow layers, which is another factor to consider when explaining the differences between the low-velocity anomalies at 25–75 m and those at 200–300 m.

In summary, our research shows that the S-wv structures obtained from dense-array ambient noise tomography can accurately reflect the characteristics of the coral reef stratum. The method successfully reflected weak geological areas (such as low-velocity and high-porosity layers) in the studied coral reef. These results support the effectiveness of this method for detecting subsurface structures in coral islands and thereby providing important references for the study of coral reef tectonic evolution and engineering construction.

4.2. Preferred frequency range for ambient noise tomography on coral reefs

Ambient noise tomography uses seismic noise to study subsurface structures; therefore, the quality of its imaging output is closely related to the characteristics of the noise source. Previous studies have shown that noise sources at low frequencies (< 1 Hz) are natural (i.e., the ocean or large-scale meteorological conditions); those of intermediate frequencies (1–5 Hz) are either natural (local meteorological conditions) or anthropogenic; and those of higher frequencies (> 5 Hz) are generally anthropogenic [51–53]. Our analyses showed that a cross-correlation of the 0.2–5.0 Hz ambient noise frequency spectrograms (Figs. 2(a)–(e)) is appropriate for coral islands. Cross-correlation functions with high SNR were extracted from the ambient noise waveform data with good symmetry (Figs. 2(f) and (g)), indicating that the 0.2–5.0 Hz noise sources were uniformly and evenly distributed

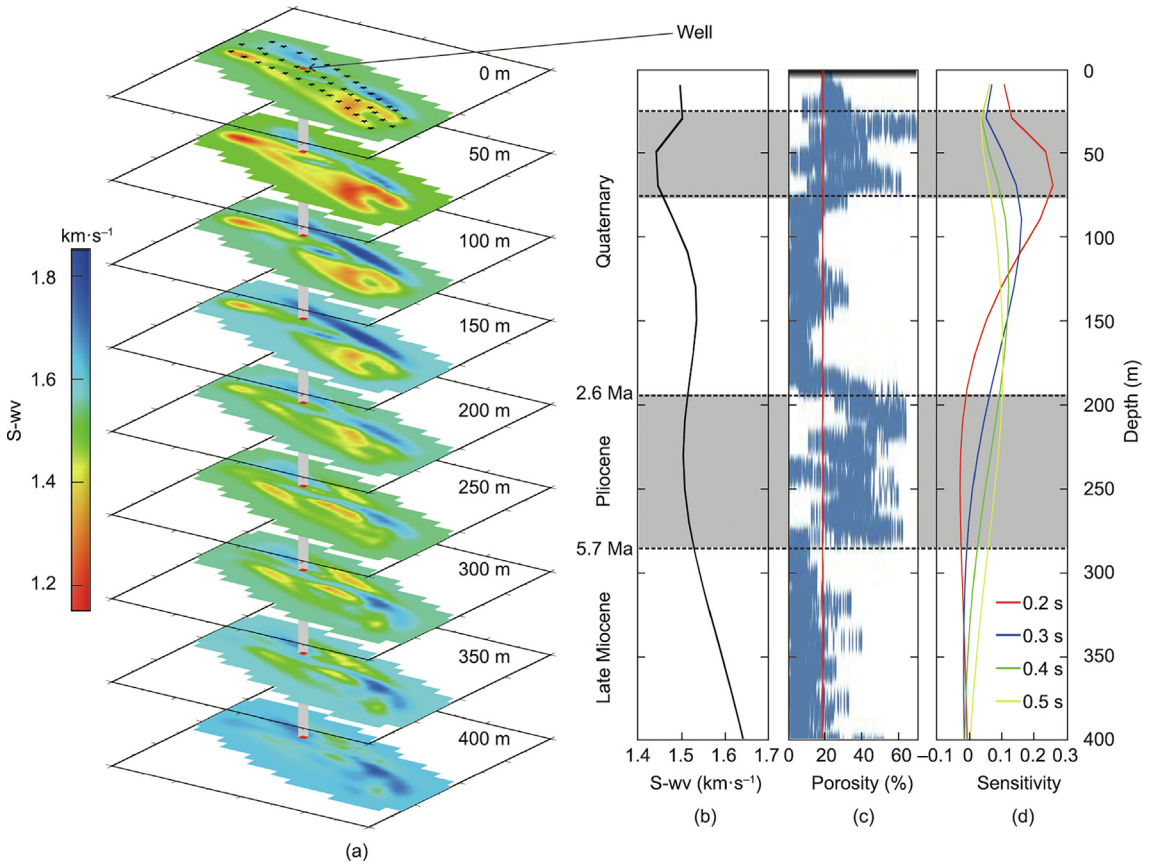

Fig. 9. (a) Horizontal slices of S-wv structures at 0–400 m. Black stars are the stations used in the inversion, and the gray column is the drilling location. (b) S-wvs at the drilling position; according to the age information of the drilling core samples, the stratum above 400 m of the studied coral reef can be divided into three periods: Quaternary, Pliocene, and Late Miocene. (c) Porosities of the drilling core samples. (d) Depth–sensitive kernels for the 0.2, 0.3, 0.4, and 0.5 s Rayleigh wave group velocity dispersions in the S-wvs.

around the coral island. Considering the fact that coral islands are far away from areas of human activity, the ambient noise below 5 Hz at the coral island was considered to have mainly natural origins and to be appropriate for use with ambient noise tomography. For the noise above 5 Hz, the ambient noise frequency spectrograms of different stations were significantly different (Figs. 2(a)–(e)). We could not effectively extract the cross-correlation functions of the corresponding frequency bands from the ambient noise (Fig. 2(h)). We propose that the above 5 Hz noise at the coral island was mainly anthropogenic and was not statistically random, because the coral island had a small population. This limits the application of high-frequency noises on coral islands for ambient noise tomography.

Although our analysis results show that the low-frequency noises (0.2–5.0 Hz) of each station on the coral island correlated well with each other (Figs. 2(a)–(e)) and that cross-correlation functions with high SNRs (Figs. 2(f) and (g)) could be obtained, it should be noted that not all low-frequency noises can be used for ambient noise tomography. This is because it is necessary to extract the dispersion curves from the noise cross-correlation functions when ambient noise tomography is based on ray theory. To ensure the reliability of the dispersion curves, the interstation distance is usually required to be greater than 1.5 times the wavelength [54,55]; that is, the lower the noise frequency is, the longer the noise wavelength will be, and the larger the required interstation distance will be. In contrast to array apertures of several hundred or even several thousand kilometers in continental regions [27,28,56], the width of a typical coral island usually ranges from only a few hundred meters to a few kilometers. The aperture of the dense array is thus limited by the size of the coral island, which in turn limits the applicability of low-frequency noises.

Taking the detection test in this study as an example, only 1–5 Hz noises could be used (Fig. 6(b)), with a corresponding maximum imaging depth of approximately 400 m (Fig. 9(d)). This was because the aperture of our array was under 2 km (Fig. 6(a)); thus, there would have been far fewer measurements with longer periods than measurements with shorter periods, which might have limited the lateral resolution of longer periods. Assuming that the Rayleigh group velocity of coral islands is 1.4 km·s^{-1} (Fig. 6(b)), the wavelength of 1 Hz noise is 1.4 km, and the corresponding minimum interstation distance is 2.1 km (1.4 km × 1.5), which is close to the size of most coral islands in the South China Sea. Therefore, attention should be paid to 1–5 Hz noises when performing dense-array ambient noise tomography on coral islands. Based on the imaging results (Fig. 9), a one-dimensional (1D) S-wv model of the coral island was established (Fig. 11(a)). Fig. 11(b) shows the depth–sensitive kernels for the 1, 2, and 5 Hz Rayleigh wave group velocity dispersions for the S-wvs. We found that the 1–5 Hz noises can reflect the S-wv structures above a depth of 800 m. For coral islands, ambient noise tomography can obtain deeper stratum structures than that by using active surface wave detection, which has an imaging depth of 25 m for such sites [12]. However, it should also be noted that the imaging accuracy of ambient noise tomography is slightly poorer because the signal frequency used is lower than that of active surface wave detection.

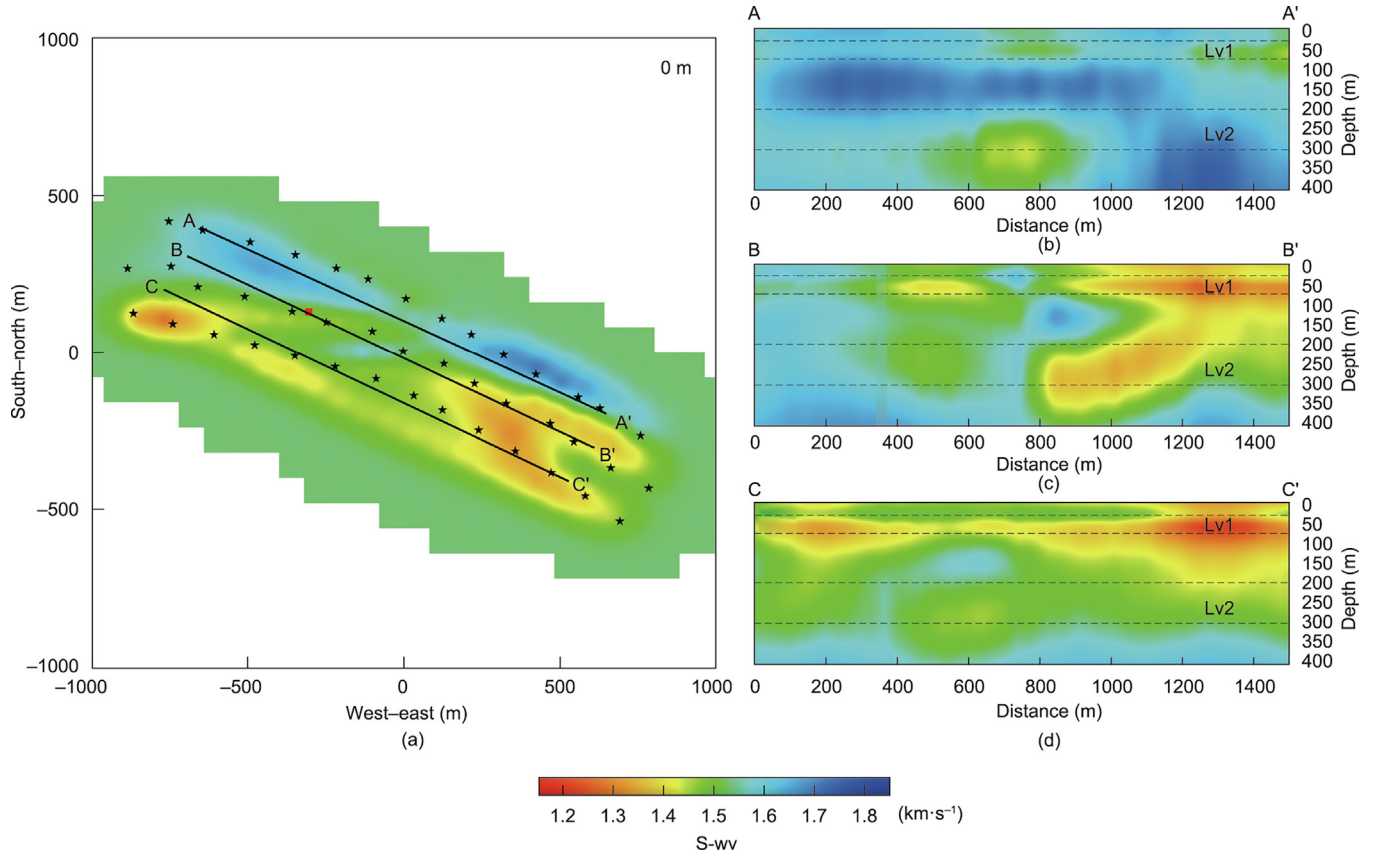

Fig. 10. (a) S-wave inversion results on the surface and the locations of three profiles; black stars represent the stations used in the inversion and the red square indicates the drilling well. (b–d) Three S-wv profiles; Lv1 and Lv2 represent two high-porosity layers found by drilling at 25–75 and 200–300 m depths, respectively, while the gray column in (c) indicates drilling.

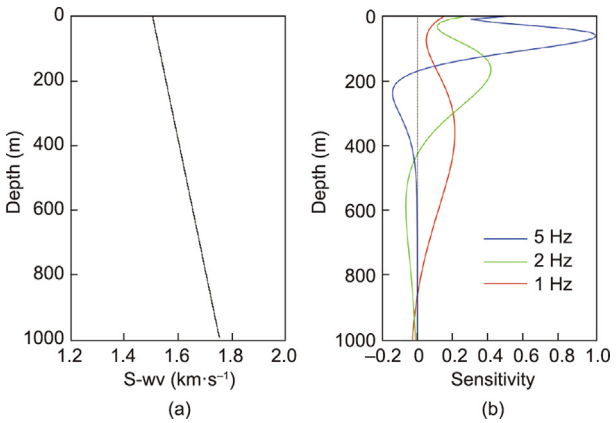

Fig. 11. (a) 1D S-wv model of the coral island; (b) depth–sensitive kernels for 1, 2, and 5 Hz Rayleigh wave group velocity dispersions for the S-wv based on the 1D model shown in part (a).

4.3. Recording time required for ambient noise tomography on coral islands

In addition to the interstation distance, the SNR of the cross-correlation functions should also reach certain thresholds, such as 3.5 [55], 5 [57], 7 [56], and 15 [29], to ensure the reliability of the dispersion curves. In addition, the more random and uniform the noise source distribution is, the closer the empirical Green's functions extracted from noise are to the real Green's functions, and the smaller the deviation of the imaging result is [58–60].

When ambient noise tomography is performed on continental regions, the SNR and symmetry of the cross-correlation functions can be improved by increasing the recording duration [38]. However, coral islands are isolated by the ocean, and the cost of field operations is high. Moreover, the humid environment of a coral island can easily cause corrosion of scientific instruments. In summer, coral islands may also be affected by extreme weather, such as typhoons, which is not conducive to the implementation of long-term observations. Fortunately, our study shows that for ambient noise below 5 Hz in the coral island, only 1-day-long waveforms are needed to extract the high SNR cross-correlation functions (Figs. 3 and 4), and the symmetry of the obtained cross-correlation functions is good (Fig. 5). This result may be due to the fact that the coral islands are small and surrounded by the sea. Thus, natural noise sources are evenly distributed around the coral island, and the propagation distances from the sources to the array are very short, limiting energy attenuation. In addition, the interference of human activities on the coral island is very small, making it possible to obtain high-quality cross-correlation functions for noise below 5 Hz by using very short waveform segments, which can greatly reduce the cost of fieldwork.

Ambient noise tomography is a passive-source detection technology with no active source required. Thus, its use can not only reduce the workload, but also minimize any potential damage to the island environment from active sources. Therefore, ambient noise tomography based on dense arrays is an economical, efficient, and environmentally friendly method for imaging the subsurface

strata structures of coral islands, and should be one of the preferred methods for future engineering geological research at such sites.

5. Conclusions

In this study, using ambient noise tomography on 5-day-long data recorded by a dense array set up on an isolated coral island in the South China Sea, we analyzed the ambient noise characteristics of the coral island and obtained a model of its 3D subsurface structure. We found that the ambient noise of isolated coral island in the ocean can be roughly divided into three categories of frequencies: < 1, 1–5, and > 5 Hz.

The spectral characteristics of noise below 5 Hz were consistent at different stations, indicating that the spectral band mainly originates from natural activities. Cross-correlation functions with a high SNR and good symmetry were obtained with only 1-day-long continuous < 5 Hz waveforms. In contrast, it was difficult to extract good cross-correlation functions for noise above 5 Hz. Finally, we were able to use a 1–5 Hz frequency band to carry out ambient noise tomography at the studied coral island because the area of the station array was small.

We revealed that the subsurface geological structure of the studied coral island had obvious zones. The S-wv of the island was higher toward the sea and lower toward the lagoon, which was consistent with the high degree of cementation of the outer-reef flat stratum on the seaward side of the island. We found two low-velocity horizons at depths of 25–75 and 200–300 m in the coral island, which were in good agreement with the high-porosity horizons revealed by drilling core samples, reflecting the multiple geological events of strata exposure and strong weathering that occurred during the development of the reef. Our research suggests that ambient noise tomography is an economical and efficient technique for obtaining the fine subsurface structure of coral islands.

Acknowledgments

The authors thank the staff of Nansha Marine Ecological and Environmental Research Station, Chinese Academy of Sciences; and Xinyang Wang, Kuiyuan Wan, Chaoyan Fan, Jiangnan Lin, and Leifeng Liu for their assistance in data acquisition. This work is supported by the Strategic Priority Research Program of the Chinese Academy of Sciences (XDA13010101), the Key Research and Development Plan of Hainan Province (ZDYF2020198), the Guangdong Research Foundation (2019BT02H594), the National Natural Science Foundation of China (42076071), the Key Special Project for Introduced Talents Team of the Southern Marine Science and Engineering Guangdong Laboratory (Guangzhou) (GML2019ZD0204), and the Rising Star Foundation of the South China Sea Institute Oceanology (NHXX2017DZ0101).

Compliance with ethics guidelines

Shaohong Xia, Changrong Zhang, and Jinghe Cao declare that they have no conflict of interest or financial conflicts to disclose.

References

[1] Zhao H, Wang L, Yuan J. Sustainable development of the coral reefs in the South China Sea Islands. Trop Geogr 2016;36(1):55–65. Chinese.
[2] An Z, Li G, Ma Y, Xu J, Ding D, Yang Z, et al. Research on coral reefal geological stability. Mark Sci 2018;42(3):113–20. Chinese.
[3] Bellwood DR, Hughes TP. Regional-scale assembly rules and biodiversity of coral reefs. Science 2001;292(5521):1532–5.
[4] Huang R, Yu K, Wang Y, Liu J, Zhang H. Progress of the study on coral reef remote sensing. Natl Remote Sens Bull 2019;23(6):1091–112. Chinese.
[5] Camoin GF, Webster JM. Coral reef response to Quaternary sea-level and environmental changes: state of the science. Sedimentology 2015;62(2):401–28.
[6] Sun Z, Zhao H. Coral reef engineering geology advancing of a new discipline. Hydrogeol Eng Geol 1998;42(1):1–4. Chinese.
[7] Kayanne H, Yamano H, Randall RH. Holocene sea-level changes and barrier reef formation on an oceanic island, Palau Islands, western Pacific. Sediment Geol 2002;150(1–2):47–60.
[8] Gischler E, Hudson JH. Holocene development of the Belize Barrier Reef. Sediment Geol 2004;164(3–4):223–36.
[9] Woodroffe CD, Webster JM. Coral reefs and sea-level change. Mar Geol 2014;352:248–67.
[10] Synolakis CE, Bardet JP, Borrero JC, Davies HL, Okal EA, Silver EA, et al. The slump origin of the 1998 Papua New Guinea Tsunami. P Roy Soc A-Math Phy 2002;458(2020):763–89.
[11] Mulia IE, Watada S, Ho TC, Satake K, Wang Y, Aditiya A. Simulation of the 2018 Tsunami due to the flank failure of Anak Krakatau Volcano and implication for future observing systems. Geophys Res Lett 2020;47(14). e2020GL087334.
[12] Cui Y, Ma L, Liu H, Huang J. Discussion on geophysical methods applied to investigation of coral island and reef. Rock Soil Mech 2014;35(S2):683–9.
[13] Walter DJ, Lambert DN, Young DC. Sediment facies determination using acoustic techniques in a shallow-water carbonate environment, Dry Tortugas, Florida. Mar Geol 2002;182(1–2):161–77.
[14] Somoza L, Ercilla G, Urgorri V, León R, Medialdea T, Paredes M, et al. Detection and mapping of cold-water coral mounds and living Lophelia reefs in the Galicia Bank. Atlantic NW Iberia margin. Mar Geol 2014;349:73–90.
[15] Saqab MM, Bourget J. Seismic geomorphology and evolution of early-mid Miocene isolated carbonate build-ups in the Timor Sea, North West Shelf of Australia. Mar Geol 2016;379:224–45.
[16] Van Tuyl J, Alves TM, Cherns L. Geometric and depositional responses of carbonate build-ups to Miocene sea level and regional tectonics offshore northwest Australia. Mar Pet Geol 2018;94:144–65.
[17] Huang X, Betzler C, Wu S, Bernhardt A, Eagles G, Han X, et al. First documentation of seismic stratigraphy and depositional signatures of Zhongsha atoll (Macclesfield Bank), South China Sea. Mar Pet Geol 2020;117:104349.
[18] Grainge AM, Davies KG. Reef exploration in the east Sengkang Basin, Sulawesi. Indonesia Mar Pet Geol 1985;2(2):142–55.
[19] Wu S, Yu K, Li X, Zhang H, Chen W. The evolution of the carbonate platforms in the South China Sea. Sci Technol Rev 2020;38(18):68–74. Chinese.
[20] Leclerc F, Feuillet N, Cabioch G, Deplus C, Lebrun JF, Bazin S, et al. The Holocene drowned reef of Les Saintes plateau as witness of a long-term tectonic subsidence along the Lesser Antilles volcanic arc in Guadeloupe. Mar Geol 2014;355:115–35.
[21] Webster JM, George NPJ, Beaman RJ, Hill J, Puga-Bernabéu Á, Hinestrosa G, et al. Submarine landslides on the Great Barrier Reef shelf edge and upper slope: a mechanism for generating tsunamis on the north-east Australian coast? Mar Geol 2016;371:120–9.
[22] Puga-Bernabéu A, Beaman RJ, Webster JM, Thomas AL, Jacobsen G. Gloria Knolls Slide: A prominent submarine landslide complex on the Great Barrier Reef margin of north-eastern Australia. Mar Geol 2017;385:68–83.
[23] Xiu C, Zhang D, Zhai S, Liu X, Bi D. Zricon U-Pb age of granitic rocks from the basement beneath the Shi Island, Xisha Islands and its geological significance. Mar Geol Quat Geol 2016;36(3):115–26. Chinese.
[24] Wu F, Xie X, Betzler C, Zhu W, Zhu Y, Guo L, et al. The impact of eustatic sea-level fluctuations, temperature variations and nutrient-level changes since the Pliocene on tropical carbonate platform (Xisha Islands, South China Sea). Palaeogeogr Palaeoclimatol Palaeoecol 2019;514:373–85.
[25] Yi L, Deng C, Yan W, Wu H, Zhang C, Xu W, et al. Neogen–quaternary magnetostratigraphy of the biogenic reef sequence of core NK-1 in Nansha Qundao. South China Sea Sci Bull 2021;66(3):200–3.
[26] Shapiro NM, Campillo M, Stehly L, Ritzwoller MH. High-resolution surface-wave tomography from ambient seismic noise. Science 2005;307(5715):1615–8.
[27] Yao H, van der Hilst RD, de Hoop MV. Surface wave array tomography in SE Tibet from ambient seismic noise and two-station analysis—I. phase velocity maps. Geophys J Int 2006;166(2):732–44.
[28] Yao H, Beghein C, van der Hilst RD. Surface wave array tomography in SE Tibet from ambient seismic noise and two-station analysis—II. crustal and upper-mantle structure. Geophys J Int 2008;173(1):205–19.
[29] Lin FC, Ritzwoller MH, Townend J, Bannister S, Savage MK. Ambient noise Rayleigh wave tomography of New Zealand. Geophys J Int 2007;170(2):649–66.
[30] Lin FC, Li D, Clayton RW, Hollis D. High-resolution 3D shallow crustal structure in Long Beach, California: application of ambient noise tomography on a dense seismic array. Geophysics 2013;78(4):Q45–56.
[31] Roux P, Moreau L, Lecointre A, Hillers G, Campillo M, Ben-Zion Y, et al. A methodological approach towards high-resolution surface wave imaging of the San Jacinto Fault Zone using ambient-noise recordings at a spatially dense array. Geophys J Int 2016;206(2):980–92.
[32] Gu N, Wang K, Gao J, Ding N, Yao H, Zhang H. Shallow crustal structure of the Tanlu Fault Zone near Chao Lake in eastern China by direct surface wave tomography from local dense array ambient noise analysis. Pure Appl Geophys 2018;176(3):1193–206.
[33] Mordret A, Roux P, Boue P, Ben-Zion Y. Shallow three-dimensional structure of the San Jacinto fault zone revealed from ambient noise imaging with a dense seismic array. Geophys J Int 2019;216(2):896–905.

[34] Yang H, Duan Y, Song J, Jiang X, Tian X, Yang W, et al. Fine structure of the Chenghai fault zone, Yunnan, China constrained from teleseismic travel time and ambient noise tomography. J Geophys Res Solid Earth 2020;125(7):e2020JB019565.
[35] Cheng F, Xia J, Ajo-Franklin JB, Behm M, Zhou C, Dai T, et al. High-resolution ambient noise imaging of geothermal reservoir using 3C dense seismic nodal array and ultra-short observation. J Geophys Res 2021;126(8). e2021JB021827.
[36] Zhou C, Xia J, Pang J, Cheng F, Chen X, Xi C, et al. Near-surface geothermal reservoir imaging based on the customized dense seismic network. Surv Geophys 2021;42(3):673–97.
[37] Garambois S, Voisin C, Romero Guzman M, Brito D, Guillier B, Refloch A. Analysis of ballistic waves in seismic noise monitoring of water table variations in a water field site: added value from numerical modelling to data understanding. Geophys J Int 2019;219(3):1636–47.
[38] Grobbe N, Mordret A, Barde-Cabusson S, Ellison L, Lach M, Seo YH, et al. A multi-hydrogeophysical study of a watershed at Kaiwi Coast (O'ahu, Hawai'i), using seismic ambient noise surface wave tomography and self-potential data. Water Resour Res 2021;57(4):e2020WR029057.
[39] Wang S, Sun X, Liu L, Zong J. Sub-surface structures and site effects extracted from ambient noise in metropolitan Guangzhou. China. Eng Geol 2020;268:105526.
[40] Yang X, Gao H, Rathnayaka S, Li C. A comprehensive quality analysis of empirical green's functions at ocean-bottom seismometers in Cascadia. Seismol Res Lett 2019;90(2A):744–53.
[41] Wolf FN, Lange D, Dannowski A, Thorwart M, Crawford W, Wiesenberg L, et al. 3D crustal structure of the Ligurian Sea revealed by ambient noise tomography using ocean bottom seismometer data. Solid Earth Discuss 2021;12:2597–613.
[42] Tian J, Lin J, Zhang F, Xu M, Zhang Y, Guo L, et al. Time correction of ocean-bottom seismometers using improved ambient noise cross correlation of multicomponents and dual-frequency bands. Seismol Res Lett 2021;92(3):2004–14.
[43] Bensen GD, Ritzwoller MH, Barmin MP, Levshin AL, Lin F, Moschetti MP, et al. Processing seismic ambient noise data to obtain reliable broad-band surface wave dispersion measurements. Geophys J Int 2007;169(3):1239–60.
[44] Schimmel M, Stutzmann E, Gallart J. Using instantaneous phase coherence for signal extraction from ambient noise data at a local to a global scale. Geophys J Int 2011;184(1):494–506.
[45] Stehly L, Campillo M, Shapiro NM. A study of the seismic noise from its long-range correlation properties. J Geophys Res 2006;111(B10):B10306.
[46] Herrmann RB. Computer programs in seismology: an evolving tool for instruction and research. Seismol Res Lett 2013;84(6):1081–8.
[47] Rawlinson N, Sambridge M. Wave front evolution in strongly heterogeneous layered media using the fast marching method. Geophys J Int 2004;156(3):631–47.
[48] Sun Z, Lu B. Elastic wave properties of coral reef rock in Nansha Islands. J Eng Geol 1999;7(2):175–80. Chinese.
[49] Zhao H, Wang L. Construction of artificial islands on coral reef in the South China Sea Islands. Trop Geogr 2017;37(5):681–93. Chinese.
[50] Luo Y, Li G, Xu W, Cheng J, Liu J, Yan W. Characteristics of Quaternary exposure surfaces in Well Nanke 1 and its relationship with sea level changes. J Trop Oceanogr 2022;41(1):15. Chinese.
[51] Gutenberg B. Microseisms. Adv Geophys 1958;5:53–92.
[52] Asten MW. Geological control of the three-component spectra of Rayleigh-wave microseisms. Bull Seismol Soc Am 1978;68(6):1623–36.
[53] Bonnefoy-Claudet S, Cotton F, Bard PY. The nature of noise wavefield and its applications for site effects studies: a literature review. Earth Sci Rev 2006;79(3–4):205–27.
[54] Li C, Yao H, Fang H, Huang X, Wan K, Zhang H, et al. 3D near-surface shear-wave velocity structure from ambient-noise tomography and borehole data in the Hefei urban area. China Seismol Res Lett 2016;87(4):882–92.
[55] Li Z, Ni S, Zhang B, Bao F, Zhang S, Deng Y, et al. Shallow magma chamber under the Wudalianchi Volcanic Field unveiled by seismic imaging with dense array. Geophys Res Lett 2016;43(10):4954–61.
[56] Yang Y, Ritzwoller MH, Levshin AL, Shapiro NM. Ambient noise Rayleigh wave tomography across Europe. Geophys J Int 2007;168(1):259–74.
[57] Liu Y, Zhang H, Fang H, Yao H, Gao J. Ambient noise tomography of three-dimensional near-surface shear-wave velocity structure around the hydraulic fracturing site using surface microseismic monitoring array. J Appl Geophys 2018;159:209–17.
[58] Yao H, van der Hilst RD. Analysis of ambient noise energy distribution and phase velocity bias in ambient noise tomography, with application to SE Tibet. Geophys J Int 2010;179:1113–32.
[59] Froment B, Campillo M, Roux P, Gouédard P, Verdel A, Weaver RL. Estimation of the effect of nonisotropically distributed energy on the apparent arrival time in correlations. Geophysics 2010;75(5):SA85–93.
[60] Delaney E, Ermert L, Sager K, Kritski A, Bussat S, Fichtner A. Passive seismic monitoring with nonstationary noise sources. Geophysics 2017;82(4):KS57–70.